IEEE Transactions on Robotics (T-RO) paper, presented at ICRA 2026, Vienna, Austria. Cite as T-RO paper.

A Multimode Motion Polar Robot: Energy-Saving Through Foldable Sail and Transformable Tracks

Yongsheng Luo, Zhaokun Guo, Tao Liu, Kaixuan Li, Jinnong Liao, Lefan Guo, Yanhe Zhu, *Senior Member, IEEE*, Gangfeng Liu, *Senior Member, IEEE*, and Jie Zhao, *Senior Member, IEEE*

***Abstract*—Existing polar robots are constrained by limited energy supply, making it difficult to carry out long-term scientific exploration missions, which highlights an urgent demand for energy conservation. An energy-efficient multimode motion polar robot is proposed to address this challenge. Both increasing external assistance and reducing the driving force are critical for lowering energy consumption. A foldable sail is designed to provide external assistance. When unfolded, the sail generates assistive force. When folded, it maintains stability in extreme polar climates. The sail shape is designed based on a symmetrically extended NACA0018 airfoil, and the influence of different sail parameters on performance is discussed. The transformable tracks realize switching between traction and sliding modes through the separation of the track and teeth chain, using the sliding mode to reduce driving force. The effect of teeth parameter variations on traction performance is analyzed. The system kinematics and dynamics are model, and stability conditions are determined. Based on this, an energy-saving motion control framework for multimode motion is proposed. Finally, experiments are conducted to evaluate the energy-saving contribution of each independent mode under different configurations. Comprehensive experiments in multimode motion demonstrate an overall energy-saving rate of approximately 24%, verifying the effectiveness of the energy-saving motion control strategy. With its energy-saving advantages, this robot shows strong potential for enabling long-term scientific exploration in polar regions.**

***Index Terms*—Energy-saving rate, foldable sail, multimode motion, polar robot, transformable tracks.**

I. Introduction

As A key regulatory region of the global climate system [1], Antarctica's unique geographical and environmental features have a profound impact on global ocean circulation [2] and energy balance. Due to the influence of the Antarctic circulation, the airflow reaching the Antarctic region is cooled and sinks, which is conducive to material deposition [3], [4]. In this extremely cold and restricted human activity area, conducting long-term and continuous scientific observations and resource exploration faces enormous challenges. There are five scientific research stations [5] along the coast and inland of Antarctica in China. Relying on robotic systems [6] to perform tasks, such as environmental monitoring and biological sampling can effectively compensate for the limitations of human work under extreme conditions.

Early polar robots were primarily powered by fuel, but due to limited energy supply, it was difficult to operate for a long time. Carnegie Mellon University has successfully developed the famous Nomad robot [7], [8], which has independently moved in the Carapace Nunatak area of Antarctica and successfully discovered five meteorites. However, due to limited fuel, Nomad is unable to carry out long-term missions. The PRISM robot developed by the University of Kansas in the United States has achieved autonomous walking on Greenland [9], [10], but due to fuel supply and storage, it is unable to perform long-distance exploration tasks. The Shenyang Institute of Automation in China has developed the fuel powered robots, which have been sent to Antarctica for testing [11], [12].

To ensure that robots do not pollute the pristine environment during observation missions in the Antarctic region [13], fuel powered polar robots are no longer considered an ideal choice [14]. Clean energy robots have become an inevitable choice for polar exploration.

Some researches have attempted to use solar energy as an energy source to drive robots. However, due to the impact of polar night, solar energy is not an ideal energy source. The pure solar powered Cool Robot developed by Dartmouth College in the United States is used for scientific research activities in Antarctica and Greenland during the summer [15], [16]. The University of Toronto and McMaster University in Canada have jointly developed the HYPERION solar robot, which has been applied to the highlands of the Canadian Arctic [17]. The wind powered spherical robot developed by NASA utilizes wind energy for propulsion [18]. But it could not achieve targeted scientific exploration due to the changes in wind direction. Beihang University has developed a robot that uses wind turbines to complete wind speed conversion [19], but the efficiency was too low in the instantaneous strong wind environment.

Overall, existing robots mainly rely on solar and wind power generation. Due to the high instantaneous wind speed in

Received 8 September 2025; accepted 27 October 2025. Date of publication 6 November 2025; date of current version 24 November 2025. This work was supported by the National Natural Science Foundation of China under Grant U21B6002 and Grant 52025054, in part by the National Defense Basic Scientific Research program of China under Grant JCKY2021203B037, in part by the State Key Laboratory of Robotics and System under Grant SKLR202102B, and in part by the PhD Candidate Innovation Fund of State Key Laboratory of Robotics and Systems under Grant SKLRS-2025-ZM-06. This article was recommended for publication by Associate Editor X. Zheng and Editor H. Zhao upon evaluation of the reviewers' comments. *(Corresponding author: Gangfeng Liu.)*

The authors are with the State Key Laboratory of Robotics and System, Harbin Institute of Technology, Harbin 150080, China (e-mail: 23B908055@stu.hit.edu.cn; 22S108250@stu.hit.edu.cn; 22B908026@stu.hit.edu.cn; 23B908035@stu.hit.edu.cn; 22B908038@stu.hit.edu.cn; 22S008081@stu.hit.edu.cn; yhzhu@hit.edu.cn; liugangfeng@hit.edu.cn; jzhao@hit.edu.cn).

This article has supplementary downloadable material available at https://doi.org/10.1109/TRO.2025.3629811, provided by the authors.

Digital Object Identifier 10.1109/TRO.2025.3629811

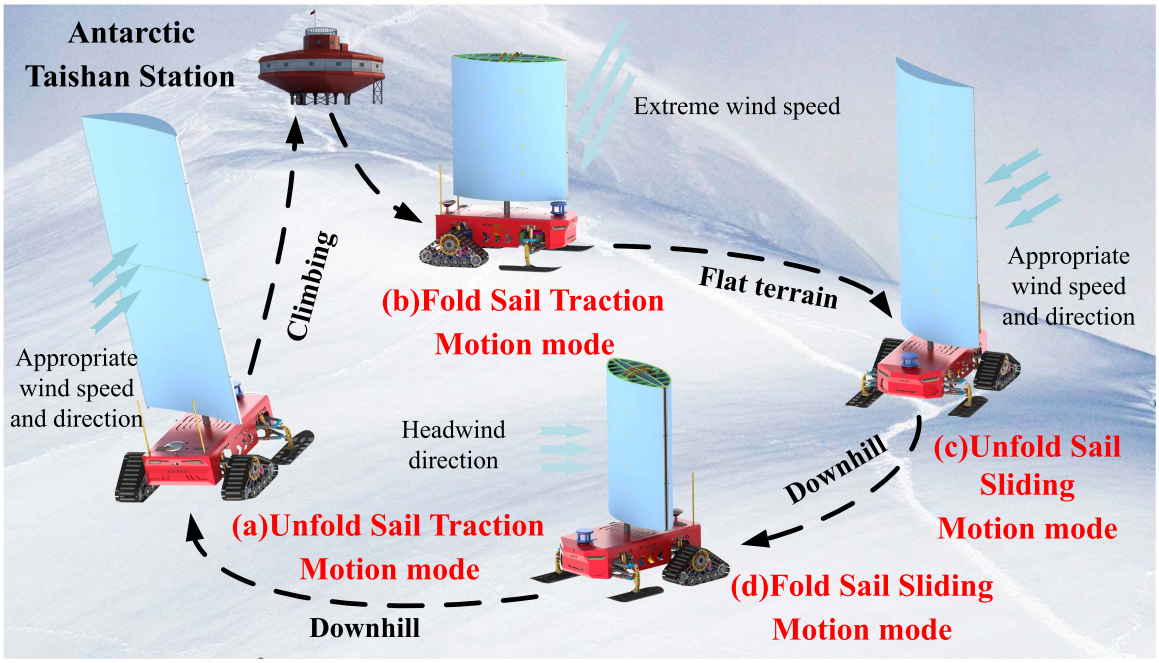

Fig. 1. Envisioned application. The Polar robot conducts high energy-efficiency scientific exploration around Taishan Station in Antarctica with its four motion modes. (a) USTM: Unfold sail traction motion mode. (b) FSTM: Fold sail traction motion mode. (c) USSM: Unfold sail sliding motion mode. (d) FSSM: Fold sail sliding motion mode.

Antarctica, the power generation efficiency is relatively low. Moreover, there is a phenomenon of polar night in Antarctica, which makes it impossible to use solar energy to meet functional requirements.

To conserve energy, it is essential to effectively utilize Antarctic wind resources to reduce robot propulsion consumption. Unlike wind turbines that convert wind into electricity, sails directly convert wind power into assistance force, thereby lowering electrical energy usage. The principle of sail assistance is analogous to the lift generated by an airplane wing. The fluid flow passing through the inner and outer surfaces of the sail is not equal. Due to unequal flow speeds over the inner and outer sail surfaces, the outer flow moves faster, resulting in lower pressure, while the inner flow remains slower with higher pressure. The pressure difference creates an aerodynamic force. By adjusting the sail angle, the force can be decomposed to maximize the forward component.

An innovative multimode motion polar robot is considered to design, which is envisioned to be applied around the Taishan Station in Antarctica for high energy-efficiency scientific exploration through four motion modes, as shown in Fig. 1. Fold sail traction motion mode (FSTM) consumes the most energy but is applicable across diverse environments. Unfold sail traction motion mode (USTM) conserves energy with sail assistance, yet requires suitable wind conditions. Fold sail sliding motion mode (FSSM) offers significantly higher energy efficiency compared to traction modes, and is generally suited for downhill terrain. Unfold sail sliding motion mode (USSM) has the highest energy-saving rate, and can rely entirely on sail assistance for sliding under suitable wind conditions. This article provides the following contributions.

1) A multimode motion polar robot for energy saving is proposed. Foldable sail is used to switch between assisted and nonassisted modes. The sail generates assistance force when unfolded and can withstand extreme wind conditions when folded. Transformable tracks are used to switch between traction and sliding modes.
2) The kinematics of steering and braking process and system dynamics are modeled. The robot stability under different terrain conditions is discussed. A energy-saving control framework for multimode motion is proposed.
3) The contribution of independent mode energy-saving rate under different configurations is discussed through field experiments. Multimotion mode comprehensive experiment was carried out to verify the effectiveness of the energy-saving control method.

The rest of this article is organized as follows. Section II introduces the design of foldable sails. Section III introduces the design of transformable tracks. Section IV introduces the system modeling and energy-saving control framework. Section V introduces experiments and analysis. Finally, Section VI concludes this article.

II. Foldable Sail Design: Assisted and Nonassisted Mode Switching

A. Design Selection

Reasonable use of sails can provide assistance during movement, which is crucial to reducing the energy consumption. Compared to soft sails, rigid sails are often easier to choose due to their excellent aerodynamic efficiency. The shape of a sail largely determines its aerodynamic characteristics. The airfoil

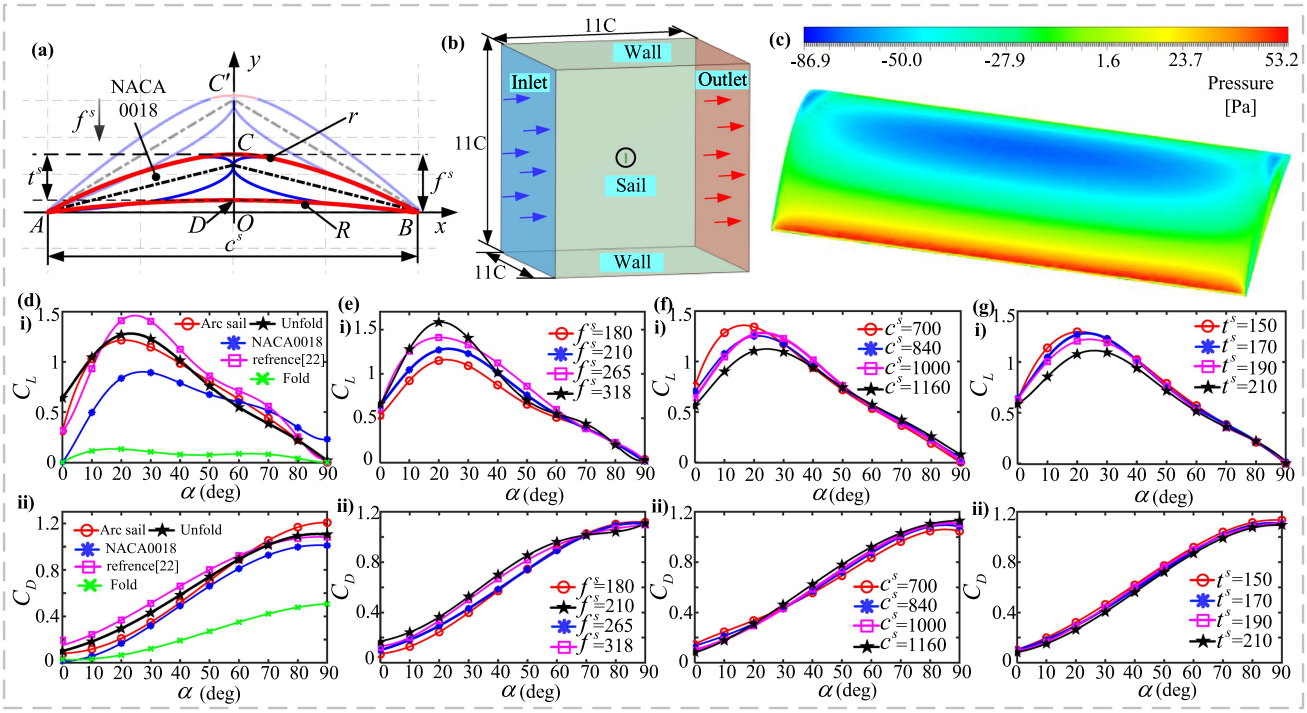

Fig. 2. Sail shape design. (a) Sail cross-sectional shape design. (b) Fluent simulation flow range setting. (c) Sail aerodynamics simulation pressure cloud map. (d) Comparison of C_L and C_D in different types of sails. (e) Comparison of C_L and C_D in different f^S. (f) Comparison of C_L and C_D in different c^S. (g) Comparison of C_L and C_D in different t^S.

developed by NACA has been widely used due to its more mature and comprehensive experimental simulation research. Unlike the greater lift required for wings, the assistance of a sail is determined by the combined force of lift and drag in the direction of robot motion. Under downwind conditions, the drag resistance generated by the sail can also serve as assistance. Therefore, NACA0018 is chosen to use as the basis for the sail design, expanding it to a symmetrical shape and passivating the wing tip and tail to achieve better assistance characteristics. Lightweight design is also an important consideration in terms of structure, materials, and other aspects.

The target of polar robot is to be applied in polar environments, which means it needs to be able to cope with various wind field environments. We have decided to design foldable sails. When facing extreme wind conditions or environmental discomfort, the sail will be folded and the robot will be in a nonassisted mode to ensure its stability. When the wind environment is suitable, the sail is deployed and the robot is in assist mode.

B. Sail Shape Design

The shape of the sail directly affects the aerodynamic characteristics of the assistance. The key sail parameters that affect the aerodynamic characteristics of wind sails include cross-sectional shape, chord length c^S, camber f^S, thickness t^S, etc. The common cross-sectional shapes of sail include arc sails, NACA series sails, and soft sails. Arc sails exhibit excellent resistance characteristics. Arc sails respond quickly to changing wind conditions, thanks to their symmetrical structural layout along the lift direction. However, due to the external leakage of its supporting skeleton and the fact that the outer surface is usually a fixed radius circular arc curve, this will affect the aerodynamic layout of the sail. NACA0018 is one of the most typical sail, with excellent performance in terms of maximum aerodynamic efficiency and minimum drag. However, because the sail needs to rotate in all directions, symmetric airfoils are particularly critical.

Combining the advantages of arc sail and NACA0018, we optimized the cross-sectional shape of the sail, as shown in Fig. 2(a). The sail adopts a symmetrical layout. The outer profile is mainly composed of two symmetrical NACA0018 sail profiles and transition end arcs. The inner surface is composed of transition arcs fitted based on the dual NACA0018 symmetric trailing edge curvature. The shape of the sail tail end has changed from a pointed sail tail to a blunt trailing edge with appropriate curvature [20]. This design approach retains the excellent aerodynamic performance of the NACA0018 airfoil profile and continues the advantages of the symmetrical airfoil in high dynamic response and variable wind fields. The structural dimensions of the sail is limited by the size requirements of the cargo box on polar transport ships. Within the limitations, we conducted a simulation analysis of the aerodynamic performance of the sail using Ansys Fluent [21]. A simulation environment 11 times larger than the sail has been set up, as shown in Fig. 2(b).

As shown in Fig. 2(d), under the same structural dimensions, the soft sail [22] lift performance exhibits more prominent lift characteristics at small angles of attack. Compared to other types of sails, NACA0018 has slightly weaker performance. Arc sails do not perform as well in terms of lift performance as the sail designed in unfolded state. The drag performance of arc sail is

TABLE I
DEFINITION AND PARAMETERS OF THE PHYSICAL VARIABLES

Symbols	Parameters	Values
f^S	Sail camber	210mm
c^S	Sail chord length	1060mm
t^S	Sail thickness	170mm
A	Windward area of the sail	2.367m^2
h_1	Height of the unfolded state of the sail	2862mm
h_3	Center height of the folded state of the sail	715.5mm
r	Track traction wheel radius	45mm
L_b	track width	200mm
k_c	Snow cohesive modulus	4.37kN/m^{n+1}
k_ϕ	Friction modulus	170.72kN/m^{n+2}
n	Sink index	1.6
c	Snow adhesion	0.52×10^3Pa
ϕ	Friction angle inside the snow	19.7°
l_{teeth}	Track teeth pitch	38mm
t_{teeth}	Track teeth height	16.5mm
b_{teeth}	Track teeth width	120mm
l_3	Distance DO in steering mechanisms	120mm
l_4	Steering linkage length	250mm

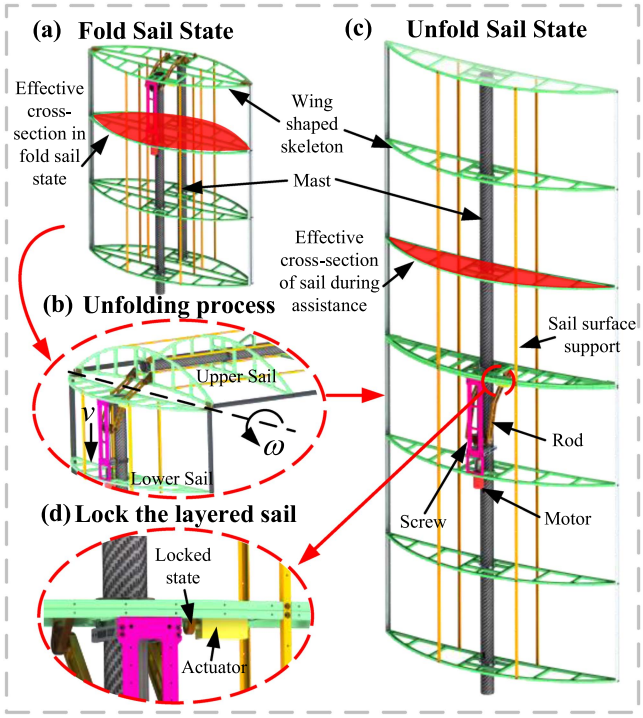

Fig. 3. Foldable sail mechanical design. (a) Sail mechanical structure in folded state. (b) Process of the sail from fold state to unfolded state. (c) Sail mechanical structure in folded state. (d) Unfold sail locks two layers of skeleton.

weak at small angles of attack, while their drag performance advantage is prominent at high angles of attack. The folded state of the sail has relatively low lift resistance, which meets the requirement of maintaining stability in strong wind environments. The aerodynamic performance of the unfolded sail is discussed in relation to changes in structural parameters. The greater the camber of the sail, the better the lift performance, as shown in Fig. 2(e). At small angles of attack, the greater the camber, the poorer the drag performance. The disadvantage of excessive camber is that it increases the weight of the sail and makes it difficult to design lightweight. An increase in chord length will reduce lift performance and improve drag performance, as shown in Fig. 2(f). Excessive chord length can also lead to excessive mass. Increasing thickness will reduce lift performance, but has little effect on drag performance, as shown in Fig. 2(g). Combining the analysis of the impact of various structural parameter changes on lift and drag performance, and ensuring lightweight design requirements, the structural size parameters of the sail are shown in Table I.

C. Mechanical Design and Model

In order to achieve lightweight design, the sail consists of an eight-layer optimized wing-shaped skeleton, mast, sail surface support, and skin, as shown in Fig. 3(c). The wing shaped skeleton is made of aluminum alloy material, which has the characteristics of light weight and high strength. Due to the large span of the wind sail chord in the longitudinal direction, the use of aluminum alloy material for wind sail surface support is used to improve the stiffness of the wind sail. The mast uses carbon fiber pipes, which are lightweight and have high toughness. It can adapt to the deflection caused by the assist process. The sail skin adopts thin carbon fiber, which is widely used as the skin material for wings and has the advantage of light weight.

The sail is divided into upper and lower layers, and the folding process of the sail is achieved through a four-bar linkage. In the folded state of the sail, it is symmetrical along the chord length direction and has a cross-sectional shape similar to an ellipse, as shown in Fig. 3(a). During the process of unfolding the sail, the motor drives the lead screw, and the nut on the lead screw drives the connecting rod to rotate the upper sail along the chord length direction, as shown in Fig. 3(b). After the sail is fully unfolded, the actuator installed on the lower sail locks the upper sail, reducing the load on the folding mechanism during the assist process.

The force relationship of the sail is shown in Fig. 4. liftF_L, dragF_D, assistance forceF_T, and lateral forceF_H can be obtained

$$F_L = \frac{C_L \rho_a {v_r}^2 A}{2}, F_D = \frac{C_D \rho_a {v_r}^2 A}{2}$$
$$F_T = \frac{C_T \rho_a {v_r}^2 A}{2}, F_H = \frac{C_H \rho_a {v_r}^2 A}{2} \quad (1)$$

where, ρ_a is the air density, v_r is the relative wind speed, which is equal to the vector superposition of the robot's forward speed v_s and absolute wind speed v_{wind}, and A is the windward area of the sail. The lift coefficient and drag coefficient C_L, C_D are obtained through Ansys Flunet simulation. C_T, C_H is the assistance force coefficient and lateral force coefficient

$$C_T = C_L \sin\varphi + C_D \cos\varphi$$

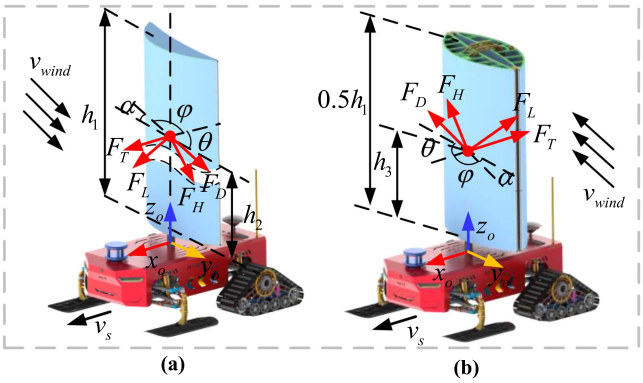

Fig. 4. Model of the sail in folded and unfolded states. (a) Force analysis of the sail in unfolded state. (b) Force analysis of the sails in folded state.

$$C_H = C_D \sin\varphi - C_L \cos\varphi \tag{2}$$

where α is attack, φ is wind direction angle, and $\alpha + \varphi + \theta = 180$. In two states, the equivalent force point and mass distribution of the sail will change. We consider the center of gravity of the sail to be in the direction of the mast axis, at h_2 when unfolded, and at h_3 when folded.

D. Assistance Performance and Fluid Structure Coupling Analysis

Based on the mechanical model of sails, the assistance force F_T and lateral force F_H are not only related to the angle of attack α but also to the wind direction angle ϕ. In practical applications, ϕ will constantly change. Therefore, the relationship between C_T, C_H of sail unfolding and folding and α and ϕ is established, as shown in Figs. 5(a) and (b). Due to the symmetrical shape of the sail, C_T, C_H also exhibits a symmetrical relationship. It is not difficult to intuitively observe that in an omnidirectional flow field, the maximum assistance force of the unfolded sail occurs in the wind direction angle range of about 90°, and the sail belongs to the small angle of attack range, which is due to the combined effect of wind lift and drag. In the folded state, the sail does not consider achieving assistance, but ensures stability. Therefore, C_H is more worthy of attention.

Sails are being considered for use in extreme climate prone environments, such as Antarctica. An analysis of the fluid coupling in sails is conducted. In the unfolded state, we conducted fluid structure coupling analysis under the conditions of v_{wind} is 10 and 20 m/s at a 90° wind direction angle. The sail is at the sail position angle corresponding to the current maximum C_T. It is not difficult to observe that at a wind speed of 20 m/s, greater assistance force and deformation are generated, but still within the resilient deformation of the mast. The unfolded state of the sail can provide assistance with a wind speed of 22 m/s. In the folded state, we conducted analysis under the conditions of v_{wind} is 40 and 60 m/s at 0° wind direction angle. The sail is at the sail position angle corresponding to the current minimum C_H. It is not difficult to find that the symmetrical distribution of folding sail can effectively cope with extreme wind speeds. Under strong winds of 60 m/s, the deformation of the mast is much smaller than the deformation limit. Therefore, reasonable control of the folding state and sail position angle can effectively adapt to strong wind environments and ensure stability.

III. Transformable Track Design: Traction and Sliding Mode Switching

A. Design Selection

In order to adapt to the complex and changing ice and snow environment in Antarctica, the robot is considered to be designed with a front snowboard guidance and rear track traction. There are many undulations and snow covered terrains in polar environments, and wheeled robots [15], [16] often sink and lose traction, while legged robots have low scientific research efficiency. Therefore, the tracks are chosen. Tracks can easily assist robots in driving or crossing icy and snowy environments, but the energy consumption generated by traction is the largest proportion in robot systems. The sled has very little resistance when sliding on ice and snow. If the track can achieve contact with the snow surface like a sled through transformation, it can rely on the downhill terrain or the assistance force generated by the sail to provide sliding driving force on the ice and snow surface. This sliding mode no longer requires tracks to provide power, relying on the front snowboard for directional control, maximizing energy savings. Therefore, we propose a transformable track with adjustable track teeth height, which separates the transmission chain between the track and the teeth. In the traction state, the track teeth extend. The robot uses battery driven tracks to achieve power traction. In the sliding state, the track teeth are retracted. The driving force is provided by sail assistance force or gravity to glide on the snow surface, with minimal energy consumption.

Meanwhile, transformable tracks have some advantages in fault recovery. When a fault is detected, the healthy track switches to traction mode to provide maximum driving force. The faulty track switches to sliding mode to reduce resistance. By using differential speed, the robot is controlled to slowly turn around the fault, adjust its posture, and leave the current fault point.

B. Mechanical Design

The overall configuration of the track is triangular, and the track chain and teeth chain are separated, as shown in Fig. 6(a). The drive wheel, guide wheel, and load-bearing wheel on the track chain are, respectively, installed on the support of the track chain. The teeth chain is installed inside the track and can move up and down along the guide slider to achieve the extension and retraction. The track chain is composed of several track shoes installed on the chain. The track shoes are designed with hollow grooves inside to facilitate the extension of the teeth. The teeth chain consists of several teeth installed on the chain and fixed on the teeth chain support.

In sliding mode, the track shoes are in direct contact with the snow surface. In order to achieve low resistance sliding, we have specially designed the material selection for the track shoes, as shown in Fig. 6(b). The track shoes are divided into three layers, with the first layer in direct contact with the snow surface

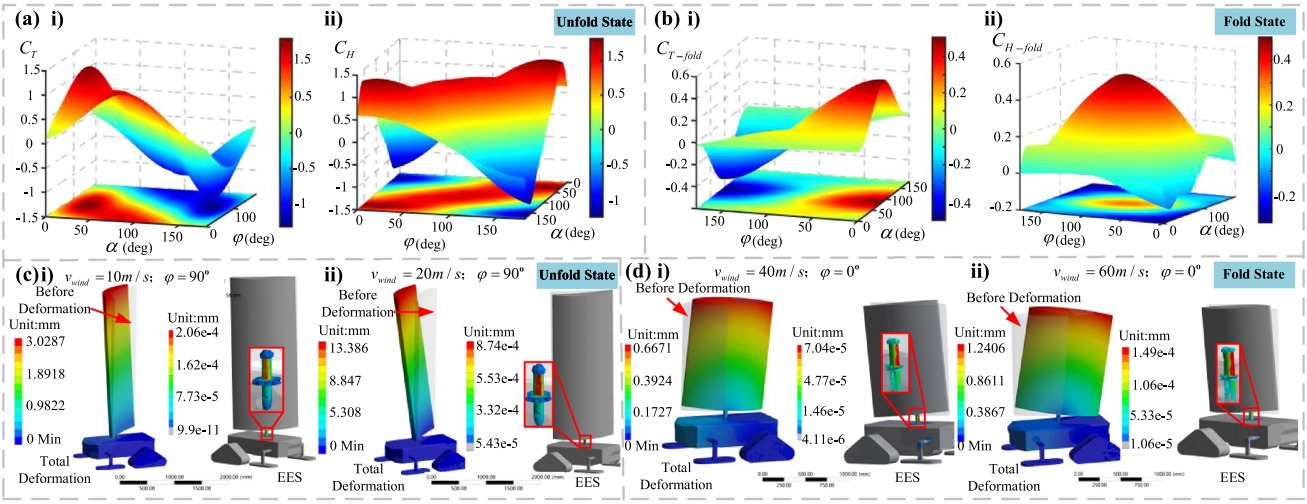

Fig. 5. Analysis of sails C_T and C_H and fluid structure coupling analysis in unfold and fold state. (a) Sail C_T and C_H in unfold state. (b) Sail C_T and C_H in fold state. (c) Deformation results of sail fluid structure coupling under maximum assistance force in unfold state, $v_{\text{wind}} = 10$ m/s, $v_{\text{wind}} = 20$ m/s. (d) Deformation results of sail fluid structure coupling under minimum force in fold state, $v_{\text{wind}} = 40$ m/s, $v_{\text{wind}} = 60$ m/s.

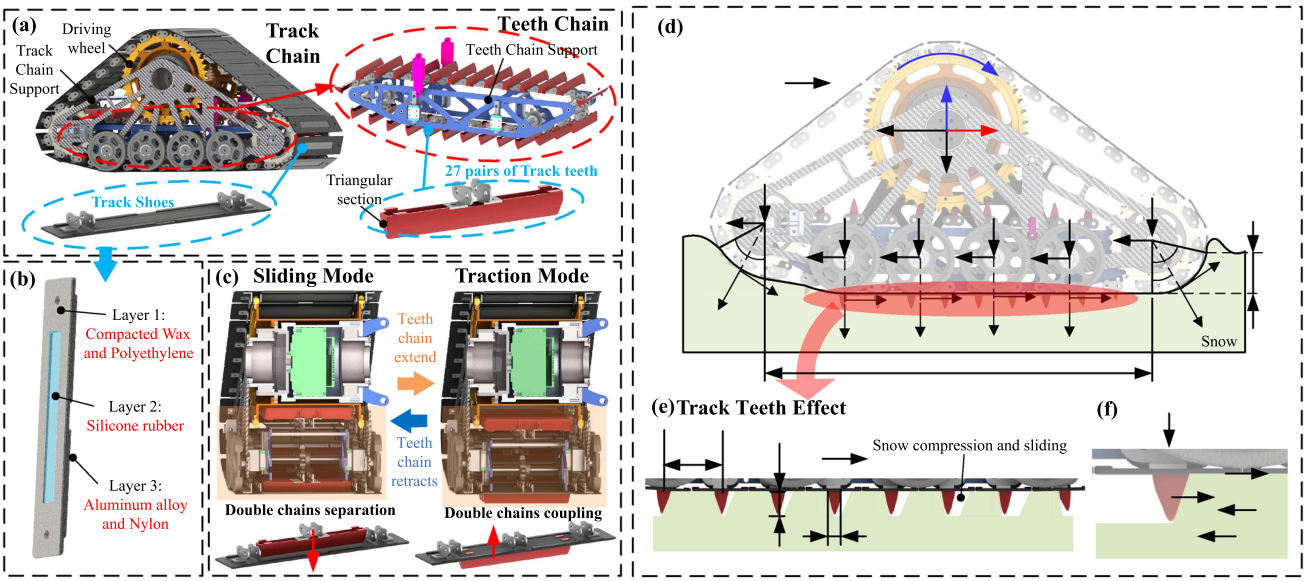

Fig. 6. Design and model of transformable tracks. (a) Mechanical design of tracks. (b) Selection of multilayer materials for track shoes. (c) Transformable track switches between sliding and traction modes by adjusting the teeth chain of the track. (d) Ground mechanics model of track traction process. (e) Analysis of the track teeth effect. (f) Force analysis of a single tooth.

being waxed and polyethylene. When the track shoes slide, an ultra-thin water film is generated due to friction. Wax can reduce hydrophilicity and prevent the water film from accumulating and forming a suction cup effect, thereby reducing the friction force during sliding. The second layer is made of silicone rubber, which is convenient for keeping the track shoes flat after the teeth retract. The third layer is made of aluminum alloy and nylon, which is lightweight and has a certain strength.

In traction mode, the driving wheels drive the track chain to move in a circular motion. Due to the extension of the track teeth from the center of the track plate, as shown in Fig. 6(c). The movement of the track chain will drive the movement of the teeth chain, forming a tangential force with the ground and driving the robot. In sliding mode, the drive wheels do not rotate, and the teeth chain retracts into the track. The two chains do not move relative to each other, ensuring that the next time the teeth chain extends, it can extend from the center of the track shoes.

C. Traction Performance Modeling and Analysis

The traction force of the track can be obtained through the ground mechanics model. The combined effect of the load-bearing and shear characteristics of snow generates normal and shear stresses at the track-snow contact point, providing support and traction for the robot. The contact between the track and the ground can be considered as the interaction between the track

shoes and the snow under the two guide wheels and the load wheels, as shown in Fig. 6(d). The traction force generated by the track guide wheels can be obtained through ground mechanics theory

$$F_{\mathrm{DP}i} = rL_b \int (\tau(\theta_i)\cos\theta - \sigma(\theta_i)\sin\theta_i)d\theta \qquad i = 1, 6 \quad (3)$$

where r is the radius of track guide wheels, L_b is the track width, and τ and σ are the shear stress and normal stress, respectively. It can be obtained [23] by

$$\begin{aligned} \sigma_i &= (k_c/b + k_\phi){z_i}^n \\ \tau_i &= (c + \sigma_i \tan\phi)(1 - e^{-j_i/K}) \end{aligned} \quad (4)$$

where k_c is snow cohesive modulus, k_ϕ is the friction modulus, z_i is the subsidence amount at wheel i, n is the sink index, c is the snow adhesion, ϕ is the friction angle inside the snow, j is the shear displacement at wheel i, which is closely related to the slip rate of the track, and K is the deformation constant of the shear curve. It should be noted that the shear stress of traction wheel 1 and traction wheel 2 varies with the change of θ. In the direction of distance L between the two traction wheels, the track shoes are evenly in contact with the snow. Within this range, the positive pressure is evenly distributed, that is, the traction force is also evenly. It is not difficult to obtain

$$F_{\mathrm{DP}i} = rb \int_0^L (c + \sigma_i \tan\phi)\left(1 - e^{-x/K}\right) dx \quad i = 2, 3, 4, 5 \quad (5)$$

where L is the length of the track contact area. However, considering only the ground mechanics shear model is not enough. The embedded teeth in the snow increase the contact area between the track and the snow, thereby increasing the shear force and improving the traction performance of the track. On the basis of Bekker's shear model, it is necessary to establish a more accurate model of the influence of the teeth structure on the traction force.

The interaction between the teeth and the snow surface is mainly divided into two stages. The first stage is the pure compression stage, in which the snow only undergoes compression without sliding. The second stage is the stable sliding stage, in which the snow completely breaks free from the clamping force of the snow on both sides and is only affected by the frictional force at the bottom of the snow, as shown in Fig. 6(e). The turning point j_k between the two stages is the critical slip point, which is related to the structural parameters of the teeth

$$j_k = \left(\frac{r_e}{k_e}\right)^{\frac{1}{n}} \left[\frac{l_{\mathrm{teeth}}}{t_{\mathrm{teeth}}}(q_b f - q_t f_s) + c\left(\frac{l_{\mathrm{teeth}}}{t_{\mathrm{teeth}}} + 2\frac{l_{\mathrm{teeth}}}{b_{\mathrm{teeth}}}\right)\right]^{\frac{1}{n}} \quad (6)$$

where, r_e is the equivalent radius of the teeth, k_e is the snow compression modulus, l_{teeth} is the track teeth pitch, t_{teeth} is the track teeth height, b_{teeth} is the track teeth width, q_b is the snow bottom pressure, q_t is the snow top pressure, and f, f_s and are the internal friction coefficient of the snow and the friction coefficient between the tread and the snow, respectively [24]. When $j > j_k$, the snow underwent stable movement, $F_{fT} = 0$. The traction force generated by the teeth is only the sum of F_{fb}, F_c, as shown in Fig. 6(f). Based on the above analysis, the traction force generated by a single tooth is

$$\begin{cases} F_{\mathrm{DPT}_i} = b_{\mathrm{teeth}} t (k_e/{r_e}^m){j_i}^n + b_{\mathrm{teeth}} l q_t f_s & j \le j_k \\ F_{\mathrm{DPT}_i} = f_{gi} F_{zb_i} & j > j_k \end{cases} \quad (7)$$

where f_g is the comprehensive friction coefficient, $f_g = f + (c/q_b)(1 + 2t_{\mathrm{teeth}}/b)$. F_{zb} is the bottom pressure of the snow. Combining Bekker's shear stress model with the traction force generated by the teeth effect, it is not difficult to obtain the total traction force generated by the entire track

$$F_{\mathrm{DP}} = \sum_{i=1}^{6} F_{\mathrm{DP}i} + \sum_{j=1}^{8} F_{\mathrm{DPT}i}. \quad (8)$$

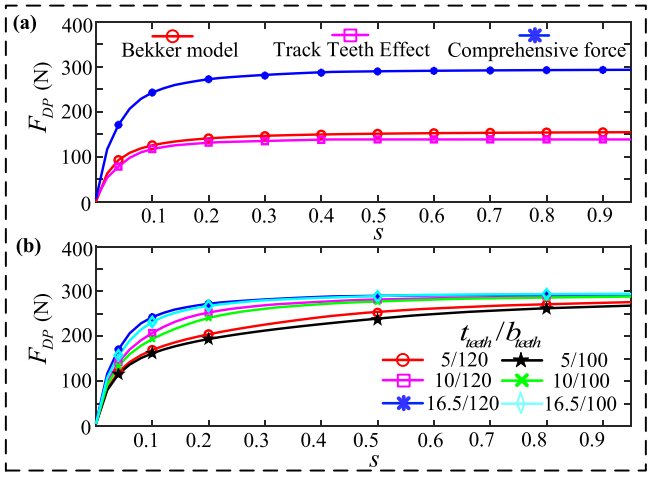

Fig. 7. Variation of traction force with the change of slip rate. (a) Variation of track traction force with slip rate under different models. (b) The variation of track traction force with slip rate under different teeth structure parameters.

The parameters related to the track configuration are shown in Table I. We calculated the traction force of the established model and obtained the variation of traction force with the change of slip rate, as shown in Fig. 7. The difference between the traction performance obtained using only the Bekker shear stress model and the performance generated by the comprehensive teeth effect model is relatively large, which directly indicates that the changes in the track teeth have a significant impact on the traction performance of the track.

The influence of different teeth parameters on the traction force of the track is analyzed, as shown in Fig. 7(b). As the depth of the teeth increases, the maximum traction force that the track can provide increases significantly, due to the more pronounced shear effect of the teeth on the snow. When designing, under the dimensional constraints between the two transmission chains, deeper teeth should be selected as much as possible to improve traction performance. The increase in the width of the teeth also slightly improves the traction performance of the track. During design, the width of the track teeth cannot be completely equal to the width of the track. While ensuring the strength of the track shoes, the width of the track teeth should be set to the maximum. In sliding mode, the teeth are retracted and the tracks do not provide traction. The track will experience sliding resistance, and its magnitude can be obtained based on (19).

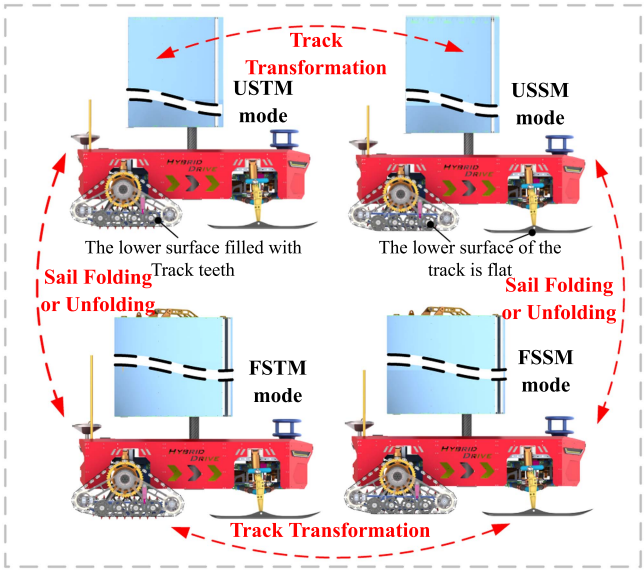

Fig. 8. Switching between the four motion modes. The transition from USTM to USSM is achieved through track transformation. The switch from USSM to FSSM is achieved through sail folding. The switch from FSSM to FSTM is achieved through track transformation. The switch from FSTM to USTM is achieved through sail unfolding.

IV. System Modeling and Energy-Saving Control Framework

A. Multimode Motion Switching

The robot has four motion modes, which are switched between by folding the sail and transforming the track, as shown in Fig. 8. By folding the sail, it is possible to switch between assisted and nonassisted modes. Transforming the tracks allows switching between traction and sliding modes. During the transition process of traction and sliding mode switching, the robot remains stationary. After completing the mode switch, the robot performs a new motion. In order to ensure the safety of the transition process, the sail position angle during the transition period is at the angle with the minimum force. Depending on terrain and wind field conditions, the robot selects the most energy-saving rate motion mode. Regardless of whether the sail is assisted or not, the energy-saving rate in sliding mode is much higher than that in traction mode. Whether in traction or sliding mode, the energy saving rate with sail assistance is improved to some extent compared to without sail assistance.

B. Kinematic Modeling of Steering Process

The direction control of the robot is achieved by adjusting the two front sleds. To ensure effective steering in multiple sport modes, human skiing movements are referenced. A steering control mechanism based on the principles of carve slip steering and plow braking has been designed. The carve slip steering process is used in various modes. During the turning process of the sleds, a standing edge angle is simultaneously generated, allowing the side blades of the sled to come into contact with the snow, thereby generating greater lateral grip. The plow brake process is used to control speed in sliding mode. By rotating and merging two sleds inward, a triangular shape is formed, while also creating a standing edge angle, increasing the contact area between the sled and the snow, significantly reducing the robot speed and achieving braking effect.

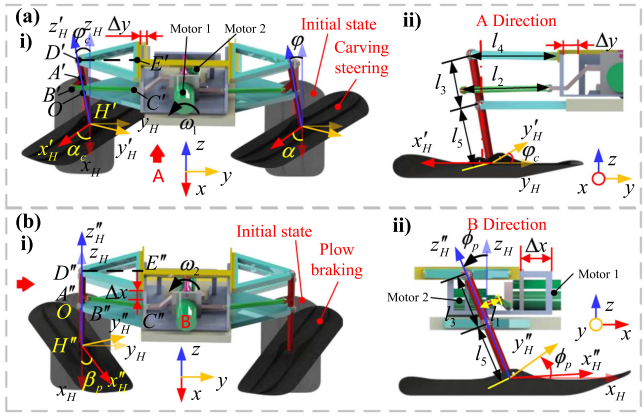

Fig. 9. Kinematic model of the carving slip steering and plow braking. (a) Kinematic model of the carving slip steering. (b) Kinematic model of the plow braking.

In order to establish a kinematic model of the mechanism's motion, we simplified the mechanism model, as shown in Fig. 9. And the following hypothesis is proposed.

1) Neglecting the small deviation between the steering angle and the edge angle caused by the clearance between the ball pairs.
2) Ignoring changes in suspension length during motion, the angle between the upper and lower fork arm suspensions and the robot body remains unchanged.

In previous studies [25], we decomposed the process of slip turning into three processes, namely the generation of standing edge angle φ_c, passive steering angle α'_c, and active steering angle α_c. The kinematic model of sled steering describes the relationship between motor input and the end of the sled. The end position and pose of the sled can be represented as follows:

$$\begin{cases} R(\varphi_c, \alpha_c) = f_1(\Delta y) \\ P(x, y, z) = f_2(\Delta y) \end{cases} \tag{9}$$

where R represents the pose of the end of the sled's vertical axis; P represents the position of the end of the sled's vertical axis, among which

$$f_1(\Delta y) =$$

$$\begin{cases} \varphi_c(\Delta y) = \arccos \frac{{l_3}^2 + A^2 - {l_4}^2}{2 l_3 A} - \arccos \frac{l_3}{A} \\ \alpha'_c(\varphi_c) = sign(\gamma(\varphi_c)) \cdot \min |\gamma(\varphi_c)| \\ \alpha_c(\Delta y) = sign(\zeta(\Delta y, \varphi_c)) \cdot \min |\zeta(\Delta y, \varphi_c)| + \alpha'_c(\varphi_c) \end{cases} \tag{10}$$

where,

$$A(\Delta y) = \sqrt{{l_3}^2 + (l_4 - \Delta y)^2}$$

$$f_2(\Delta y)=\begin{bmatrix}1 & 0 & 0\\ 0 & \cos\varphi_c(\Delta y) & -\sin\varphi_c(\Delta y)\\ 0 & \sin\varphi_c(\Delta y) & \cos\varphi_c(\Delta y)\end{bmatrix}\begin{bmatrix}x_H\\ y_H\\ z_H\end{bmatrix}. \quad (11)$$

According to the above decomposition principle, the plow braking process can also be decomposed into three processes, namely the generation of the vertical blade angle ϕ_p, the generation of the passive brake angle β_p', and the generation of the active brake angle β_p. The process of generating φ_p is due to the movement Δx of the upper fork arm. According to geometric relationships

$$\phi_p=\arcsin\frac{\Delta x}{l_3}. \quad (12)$$

The principle of passive braking angle generation is similar. During the process of vertical blade angle generation, the sled should have remained parallel to the direction of the forward movement. The position of point A has changed, but the rack has not moved, while the position of point C remains unchanged. Due to the length limitation of the steering link BC, the vertical axis of the sled actually rotated [26]

$$\beta_p{}'=\min\left|\arctan\frac{\omega^T(u'\times v')}{u'^Tv'}\pm\arccos\frac{\|u'\|^2+\|v'\|^2-\delta'^2}{2\|u'\|\|v'\|}\right| \quad (13)$$

where $u=(B'-O)$, and $v=(C'-O)$.

During the process of generating the active braking angle, the brake rack moved Δy_2 causing point C to move to point C''. The steering link BC performs spatial motion, causing the sled to rotate β_p around $D''H''$

$$\beta_p=\min\left|\arctan\frac{\omega^T(u'\times v')}{u'^Tv'}\pm\arccos\frac{\|u'\|^2+\|v'\|^2-\delta'^2}{2\|u'\|\|v'\|}\right| \quad (14)$$

where $u=(B''-O)$, and $v=(C''-O)$.

Based on the analysis of the plow braking process mentioned above, the geometric relationship between the sled end posture and the motor input is mapped as follows:

$$\begin{cases}R(\phi_p,\beta_p)=f_1(\Delta x,\Delta y_2)\\ P(x,y,z)=f_2(\Delta x)\end{cases} \quad (15)$$

where

$$f_1(\Delta x,\Delta y_2)=\begin{cases}\phi_p(\Delta x)=\arcsin\frac{\Delta x}{l_3}\\ \beta'_p(\phi)=\min|\gamma(\phi)|\\ \beta(\Delta x,\Delta y_2)=\min|\zeta(\Delta y',\phi_p)|+\beta'_p(\phi_p)\end{cases} \quad (16)$$

$$f_2(\Delta x)=\begin{bmatrix}\cos\phi_p(\Delta x) & 0 & \sin\phi_p(\Delta x)\\ 0 & 1 & 0\\ -\sin\phi_p(\Delta x) & 0 & \cos\phi_p(\Delta x)\end{bmatrix}\begin{bmatrix}x_H\\ y_H\\ z_H\end{bmatrix}. \quad (17)$$

C. Model Analysis and Stability

1) *Dynamics Model:* The coordinate system during the motion of the robot is defined, as shown in Fig. 10. $\{O-XYZ\}$ is the world coordinate system. $\{o_i-x_iy_iz_i\}, i\in[1,4]$ is the accompanying coordinate system for robot tracks and sleds. $\{o_F-x_Fy_Fz_F\}$ is the sail coordinate system, and $\{o_R-x_Ry_Rz_R\}$ is robot coordinate system. The robot dynamics model can be represented as

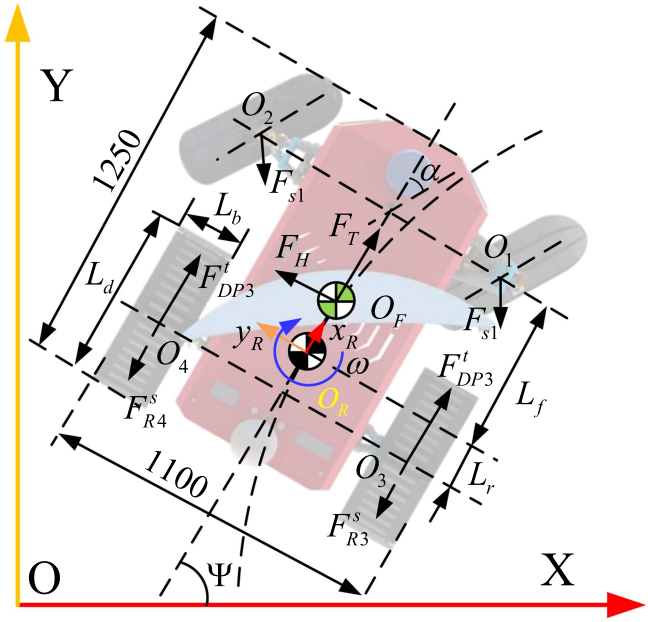

Fig. 10. Polar robot dynamics model.

$$m\ddot{p}=\sum_{i=1}^{2}\begin{bmatrix}\cos\alpha_c & \sin\alpha_c & 0\\ \sin\alpha_c & -\cos\alpha_c & 0\\ 0 & 0 & 1\end{bmatrix}F_{si}$$
$$\sum_{i=3}^{4}F_{si}+\sum_{i=3}^{4}F^t_{\mathrm{DP}i}+{}^FR_R\begin{bmatrix}F_T\\ F_H\\ 0\end{bmatrix}+\begin{bmatrix}G\sin\delta\\ 0\\ G\cos\delta\end{bmatrix}$$
$$I\dot{\omega}=\sum_{i=1}^{2}M_{q_i}+M_F \quad (18)$$

where $\ddot{p}=[x\quad y]^T$, F_{si} is the resistance of the sled against the snow surface, $F^t_{\mathrm{DP}i}$ is the traction force provided by the tracks, M_{q_i} is the steering resistance torque [27], M_F is the torque of the sail on $\{o_R-x_Ry_Rz_R\}$, and ${}^FR_R$ is the transformation matrix from $\{o_F-x_Fy_Fz_F\}$ to $\{o_R-x_Ry_Rz_R\}F_{si}$ can be obtained through the infinitesimal method [28]

$$F_{si}=\begin{bmatrix}\int_{-L_d/2}^{L_d/2}\int_{-L_b/2}^{L_b/2}\mu p\frac{y}{\sqrt{x^2+y^2}}\cos\varphi_c dx_i dy_i\\ \int_{-L_d/2}^{L_d/2}\int_{-L_b/2}^{L_b/2}\mu p\frac{x}{\sqrt{x^2+y^2}}\cos\varphi_c dx_i dy_i\\ 0\end{bmatrix} \quad (19)$$

where μ is the resistance coefficient, which can be obtained through the empirical formula in [24], and p_i is the ground pressure

$$p_{1,2}=\frac{mgL_r}{2L_dL_b(L_r+L_f)}\quad p_{3,4}=\frac{mgL_f}{2L_dL_b(L_r+L_f)} \quad (20)$$

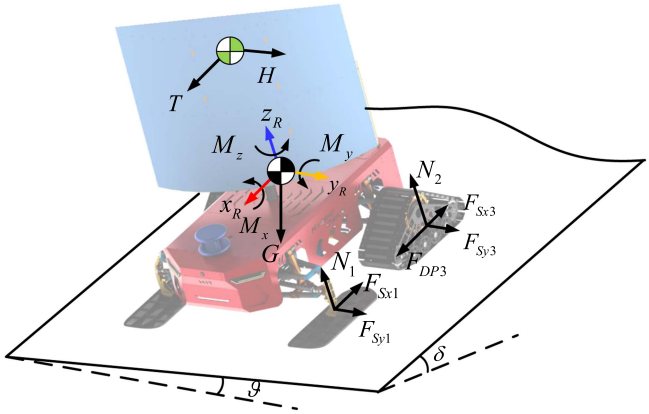

Fig. 11. Stability analysis of polar robot.

where L_r, L_f represents the distance between the mass center of the robot and the centers of the tracks and sleds, respectively.

2) *Impact of Payload and Mass Distribution:* It is not difficult to find that the payload and mass distribution of robots directly affect the ground pressure p_i. When the payload of the robot increases, p_i and F_{si} increase accordingly. In traction mode, the tracks need to provide greater driving force, resulting in increased energy consumption. In sliding mode, the track is more similar to a sled, subject to resistance from the snow surface. The increase in payload will lead to an increase in the resistance of robot sliding, which means that greater sail assistance force or gravitational force is needed.

When the quality distribution of the robot changes, L_f, L_r will change accordingly, which leads to differences between the p of sleds and tracks. In traction mode, when L_r is too large, which means the center of mass is close to the front sled with $p_{3,4}$ decrease. This directly results in a decrease in the depth of track sinking and insufficient maximum traction force that can be provided. On the contrary, when the center of mass approaches the track, the maximum traction force that the track can provide will increase. In sliding mode, the change in mass distribution has little effect on straight-line sliding. However, during the steering process, the center of mass moving forward leads to understeer, while moving backward causes drift.

3) *Stability Analysis:* In the actual driving process of robots, it is necessary to consider the quasi-static stability constraints of motion, such as the risk of overturning of robots in strong crosswinds and the risk of overturning caused by changes in ground slope. The force situation of the robot is shown in Fig. 11. Among them, the torque equation

$$\begin{cases} M_x = \sum N_i y_i + \sum F_{syi} z_i + F_H h_1 \\ M_y = \sum N_i x_i + \sum F_{sxi} z_i - \sum F_{\mathrm{DP}i} z_j + F_T h_1 \\ M_z = \sum F_{sxi} y_i + \sum F_{syi} x_i. \end{cases} \tag{21}$$

During the normal operation of the robot, it is necessary to ensure that both the sled and tracks on either side are in contact with the ground. In the yoz plane, the stability condition is

$$\begin{cases} \lambda_{lf} = \left(\frac{G x_{O1} \cos\vartheta}{L_d A_s} - \frac{M_x}{W_{xs}} \right) > 0 \\ \lambda_{lr} = \left(\frac{G x_{O3} \cos\vartheta}{L_d A_t} - \frac{M_x}{W_{xt}} \right) > 0. \end{cases} \tag{22}$$

In the xoz plane, the stability condition is

$$\lambda_{lr} = \lambda_{rr} = \left(\frac{G \cos\delta}{2A_t} - \frac{M_y}{W_y} \right) > 0 \tag{23}$$

where x_{O1}, x_{O3} is the distance between the sled, track, and center, and A_s, A_t is the equivalent compression area of the sled and tracks. W_{xs}, W_{xt}, W_y is the bending section modulus of the sled and track along the x or y direction.

Through the above analysis, the maximum overturning moment $M_{x\max}, M_{y\max}$ that the robot can withstand during stable driving can be calculated. To ensure the safety of robots under conditions, such as steering and suspension compression, the safety factor k_x, k_y is introduced to provide a certain margin of stability

$$\begin{cases} M_x \le k_x M_{x\max} \\ M_y \le k_y M_{y\max}. \end{cases} \tag{24}$$

D. Energy Saving Motion Control Framework

An energy-saving motion control framework is proposed, as shown in Fig. 12. The user sends the expected speed v^d and heading angle Ψ^d. The wind sensor is installed at the front of the robot to measure wind speed v_w and wind direction angle φ in real time. The sail solver is used to calculate the optimal sail position angle in the current wind environment. It includes stability constraints and a sail position angle solver in folding or unfolding mode. The motion mode selection module combines expected commands and sensor information to calculates and selects the motion mode. Expected motion information and sail information input into the dynamic model to calculate the required motor force, steering angle, braking angle, and other information. PD controllers are used to control the actions of robot actuators. The sensor feedback data carried on the robot is fed back to the previous module through the state estimator.

1) *Energy-Optimal Sail Position Angle Solver:* The sails are in either unfolded or folded states, and there are different methods for solving the sail position angle. First, it is necessary to determine whether the robot meets the stability constraint. If it does not meet the stability constraint, the sail needs to be folded. This means that the robot is in a harsh environment, and the solver needs to find the most stable sail position angle. If the stability constraint is met, the sail needs to be unfolded and in assist mode, and the solver needs to find the most energy-efficient sail position angle. In a headwind environment, where the wind direction angle is approximately within $\pm 30^\circ$, regardless of how the sail position angle is adjusted, the sail cannot provide assistance. It is still necessary to choose to fold the sail.

In the unfolded state, the sail needs to provide the maximum assistance force for the robot to minimize the driving force of track traction or provide driving force in sliding mode. In previous research, we proposed a sail-assisted strategy [25] that

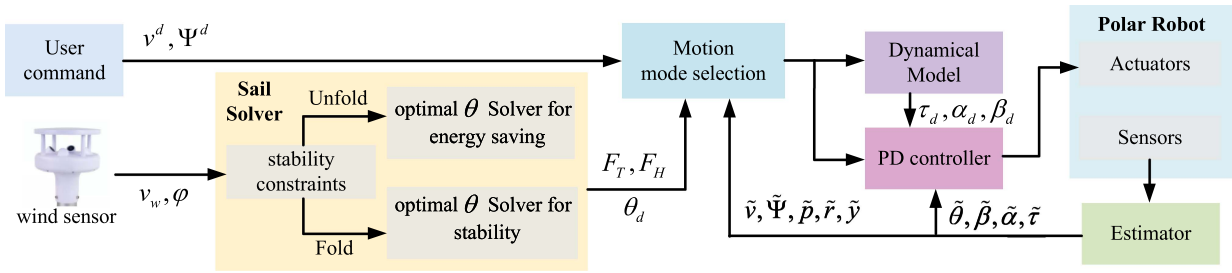

Fig. 12. Energy saving motion control framework. The sail solver is used to calculate F_T, F_H, and θ_d. The motion mode selection module calculates and selects the motion mode. Dynamic model calculates the required control information. PD controllers control the actions of robot actuators.

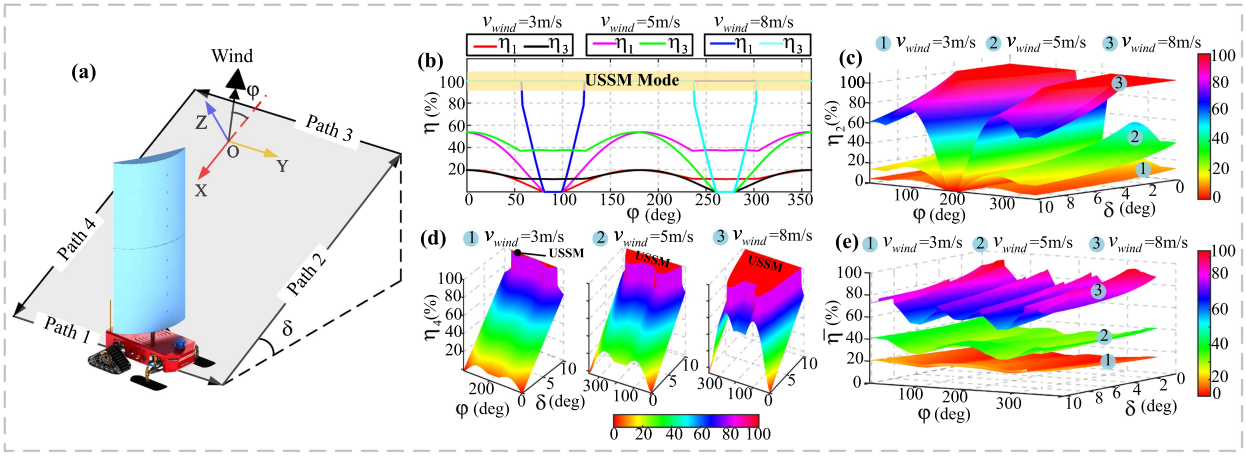

Fig. 13. Simulation analysis based on energy-saving control framework. (a) Simulation scene settings with four paths. (b) Impact of φ change on the energy-saving rate η_1 of path1 and the energy-saving rate η_3 of path 3. (c) Impact of φ and δ change on the energy-saving rate η_2 of path 2. (d) Impact of φ and δ change on the energy-saving rate η_4 of path 4. (d) Impact of φ and δ change on the average energy-saving $\bar{\eta}$.

obtains the maximum assisted assistance force while ensuring the stable operation of the robot. This strategy is constrained by the stability of the robot's motion and the range of sail position angle motion, and solves for the maximum assisted assistance force and corresponding sail position angle

$$\begin{cases} \max & F_T(\varphi, \alpha) \\ & M_x \le k_x M_{x\max} \\ s.t. & M_y \le k_y M_{y\max} \\ & \varphi, \alpha \in [0, 180]. \end{cases} \tag{25}$$

In the folded state, the sail still receives assistance force $F_{T-\text{fold}}$ and lateral force $F_{H-\text{fold}}$. The force situation varies at different sail position angles. To ensure stability, it is necessary to ensure that the sail position angle is at the angle where the external force is minimized. At this sail position angle, the resistance to the robot's motion is minimized, achieving the goal of saving energy consumption. Under the lateral force performance of wind sail folding, as shown in Fig. 5(b), establish the following method for solving the sail position angle:

$$\begin{cases} \min & |F_{T-\text{fold}}(\varphi, \alpha) + F_{H-\text{fold}}(\varphi, \alpha)| \\ & M_x \le k_x M_{x\max} \\ s.t. & M_y \le k_y M_{y\max} \\ & \varphi, \alpha \in [0, 180]. \end{cases} \tag{26}$$

2) *Motion Mode Selection:* In the sail solver, the folded or unfolded state of the sail and the corresponding F_T, F_H, θ_d have been obtained. In the selection of motion mode, the first step is to determine whether the robot can switch to sliding mode. Substitute F_T, F_H, θ_d into (18) to solve for the required track traction force. The slope angle δ in the environment can be approximated by the roll angle r of IMU. If $F_{\text{DP}} \le 0$, switch to sliding mode. If $F_{\text{DP}} > 0$, it indicates that the robot still needs tracks to provide a certain amount traction force. The motion mode selection module outputs the desired motion mode for the robot. Using the dynamics solving module, determine the corresponding control parameters.

E. Simulation Analysis

To validate the proposed energy-saving motion control framework, a rectangular sloping environment is envisioned. The robot moves along a rectangle with a total of four paths, as shown in Fig. 13(a). The paths for flat driving are path 1 and path 3, path 3 for uphill driving, and path 4 for downhill. The motion speed of the robot is 1 m/s. We obtained the relationship between the energy-saving rate of robots and changes in wind direction, wind speed, and slope through simulation calculations. The wind speed is set to 3, 5, and 8 m/s. The range of wind direction angle is set from $0 - 360°$. The range of slope change is set to $0 - 10°$.

TABLE II
TECHNICAL SPECIFICATIONS OF POLAR ROBOT

System	Parameter	Value
Mechanical System	Sail mass	15 kg
	Track mass	23 kg
	Sled mechanism mass	12 kg
	Body mass	30 kg
Sampling System	Wind sensor	20 Hz
	IMU	200 Hz
	Motor	200 Hz
Power System	Temperature range	-40° C to 60° C
	Capacity	35 Ah (64 V)

FSTM is the most energy consuming mode among the four motion modes, but it can adapt to all environments. Therefore, the energy-saving rate of the motion mode is calculated relative to the FSTM mode. The energy-saving rate of robots is defined as

$$\eta = \frac{W - W_{\text{FSTM}}}{W_{\text{FSTM}}} \times 100\% \tag{27}$$

where W is the energy consumption under multiple motion modes, and W_{FSTM} is the energy consumption under FSTM.

Due to the flat terrain of paths 1 and 3, slope changes have little impact on energy-saving rate. The impact of φ change on the energy-saving rate η_1 of path 1 and the energy-saving rate η_3 of path 3 is shown in Fig. 13(b). As the wind speed increases, the energy-saving rate gradually improves. When the wind speed reaches 8 m/s, the robot is mostly in sliding mode, with an energy-saving rate of about 100%. The energy-saving rate η_2 of path 2 is shown in Fig. 13(c). It is quite evident that an increase in wind speed leads to a significant improvement in η_2. When φ is around 180°, the robot moves completely against the wind and cannot use the sail, which η_2 is 0. As δ increases, η_2 gradually decreases. The greater the slope, the greater the traction required by the robot. The energy-saving rate η_4 of path 4 is shown in Fig. 13(d). An increase in wind speed will also significantly enhance η_4. It is worth noting that as δ increases, η_4 always remains greater than 0. This is the result of the combined action of sliding mode and sail assistance. As δ increases, η_4 gradually approaches 100% and switches to sliding mode. The higher the wind speed, the easier it is to meet the sliding mode conditions. Weighted four paths to obtain the average energy-saving rate

$$\bar{\eta} = \frac{1}{4}(k_e\eta_e + k_n\eta_n + k_w\eta_w + k_s\eta_s). \tag{28}$$

The results of the variation of $\bar{\eta}$ with wind speed, δ, and φ are shown in Fig. 13(d). $\bar{\eta}$ is sensitive to wind speed. An increase in wind speed will significantly increase $\bar{\eta}$.

V. EXPERIMENTS AND ANALYSIS

The technical parameters of polar robot are shown in Table II. The robot mainly consists of five subsystems: 1) motion control system; 2) sensing system; 3) power management system; 4) wireless communication system; and 5) temperature control system.

A. Experimental Design

In order to verify the ability of the robot to traverse multiple terrains, we tested the robot motion ability to traverse different terrains, such as snow surfaces with varying degrees of compaction, mixed snow and ice surfaces, and ice cracks. The experiment can be seen through the supplementary video.

In order to verify the energy saving motion control framework for multimode motion, we conducted experiments on field ice and snow surfaces. In order to verify the effects of sail assistance and traction, sliding mode on energy saving rate improvement, respectively, energy-saving experiments in four independent modes separately is conducted. We have designed independent motion mode energy-saving experiments for robots in flat, climbing, and downhill terrains, which intuitively demonstrate the impact of terrain changes on energy-saving rates.

Finally, in order to verify the energy-saving rate of the robot operating in multiple motion modes, we designed a rectangular ramp scene similar to the simulation. We compared the changes in energy-saving rate of robots under multiple motion modes to further verify the effectiveness of the designed robot and energy-saving control method.

In the experiment, the energy-saving rates in each mode are defined by comparing with the FSTM which is the highest energy consumption. Define the energy-saving rate at a certain moment as the instantaneous energy-saving rate

$$\eta_{\text{ins}}(t) = \frac{I_{\text{FSTM}}(t) - I(t)}{I_{\text{FSTM}}(t)}. \tag{29}$$

The energy-saving rate of each mode during the entire movement process is also compared with FSTM. Define the energy-saving rate of the entire motion process as the comprehensive energy-saving rate

$$\eta_{\text{com}} = \frac{\sum_{i=0}^{n}\left(I_{\text{FSTM}}(nt_k) - I(nt_k)\right)}{\sum_{i=0}^{n} I_{\text{FSTM}}(nt_k)}. \tag{30}$$

B. Energy Saving Experiment in Independent Mode Under Different Terrains

1) *Flat Terrain Experiment:* To verify the effect of sail assistance on energy efficiency, we controlled the robot to move along a flat rectangle under FSTM and USTM, as shown in Fig. 14(a) and (b). The robot's speed was about 1 m/s. The robot's motion path includes a total of four straight paths.

We collected trajectory and yaw angle information in two modes, as shown in Fig. 14(c). The position, speed, and yaw angle of the motion are almost the same in both modes. The wind direction and speed under USTM was collected through wind direction sensor, as shown in Fig. 14(d). The maximum sail assistance force at each wind direction angle corresponds to the sail position angle information was provided. It was not difficult to see that the trend of sail position angle changes was consistent with the change of wind direction angle, basically between 120° and 160°. During experiment, the maximum assistance force of the sail was about 27 N. As the wind speed changes, the sail

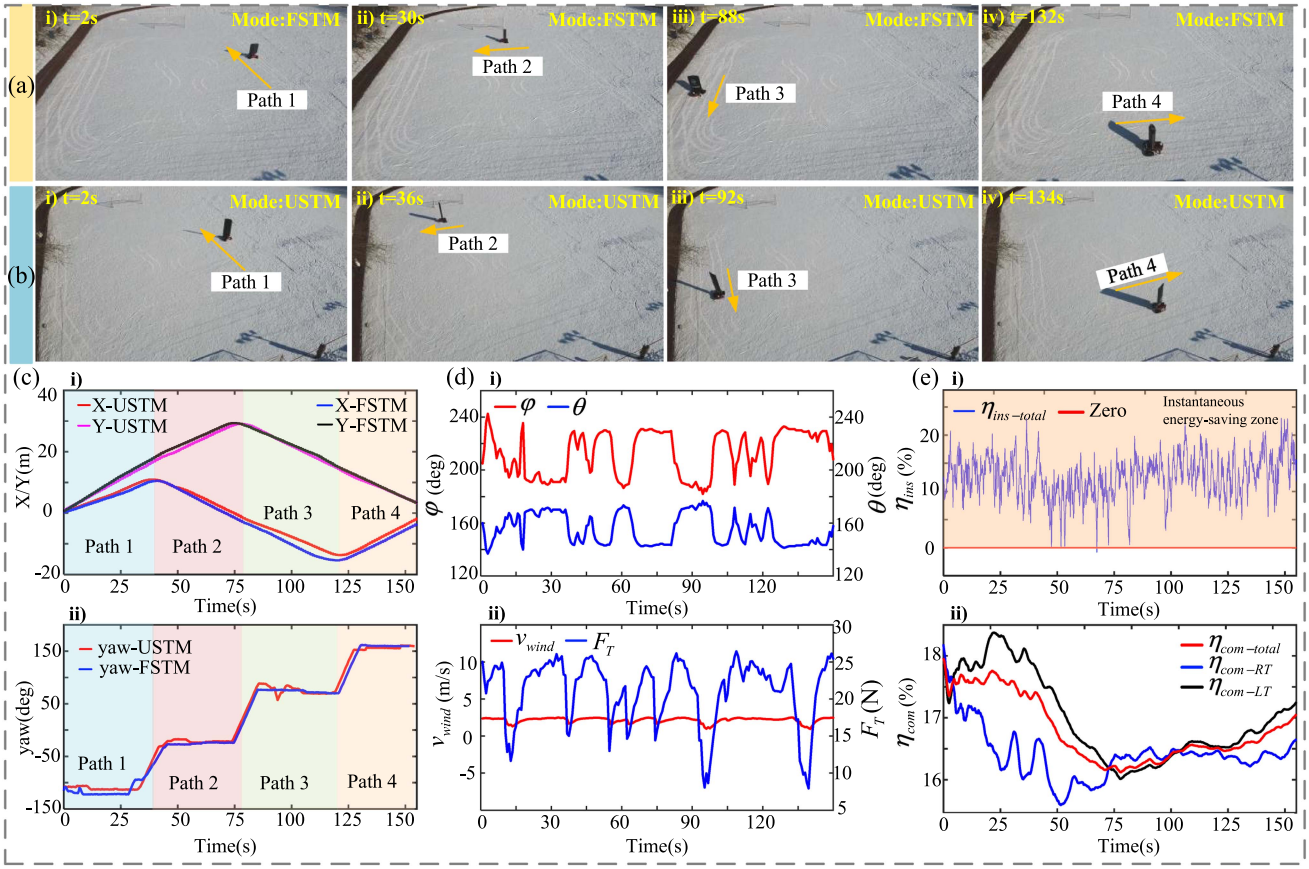

Fig. 14. Flat terrain experiment results. (a) Process of flat terrain motion under FSTM. (b) Process of flat terrain motion under USTM. (c) Trajectory and yaw angle information in FSTM and USTM. (d)(i) Wind direction and corresponding sail position angles under USTM. (d)(ii) Wind speed and corresponding sail assistance force under USTM. (e)(i) Variation of instantaneous energy-saving rate η_{ins}. (e)(ii) Variation of the comprehensive energy-saving rate $\eta_{\text{com}-\text{total}}$, $\eta_{\text{com}-\text{RT}}$, $\eta_{\text{com}-\text{LT}}$.

assistance force fluctuated between 10 and 27 N and followed the trend of wind speed.

Fig. 14(e)(i) shows the variation of instantaneous energy-saving rate. The instantaneous energy-saving rate was basically within the instantaneous energy-saving zone throughout the entire motion process, $\eta_{\text{ins}} > 0$. This indicates that at every moment, the sail provides assistance, thereby reducing the energy consumption required for track drive. The instantaneous energy-saving rate η_{ins} basically maintained between 0 and 20%.

Fig. 14(e)(ii) shows the variation of the comprehensive energy-saving rate. $\eta_{\text{com}-\text{total}}$, $\eta_{\text{com}-\text{RT}}$, and $\eta_{\text{com}-\text{LT}}$, respectively, represent the overall comprehensive energy-saving rate of the robot, the comprehensive energy-saving rate of the right track, and the comprehensive energy-saving rate of the left track. Throughout the entire movement, $\eta_{\text{com}-total}$ remained stable between 16% and 18%, with a comprehensive energy-saving rate of 17.1%.

2) *Climbing Terrain Experiment:* We controlled the robot to climb slopes under FSTM and USTM, respectively, as shown in Fig. 15(a) and (b). The slope was 8°. The robot's movement speed was about 1 m/s. The wind direction and speed information were collected, as shown in Fig. 15(c).

During the climbing process, the wind direction did not change significantly, ranging from 145° to 165°. The corresponding range of sail position angle changes was also not large. The wind speed was generally between 1.5 and 2.5 m/s. The maximum sail assistance force was about 30 N. The instantaneous energy-saving rate in Fig. 15(c)(i) was mostly within the instantaneous energy-saving region. At certain times, USTM was not energy-efficient, which may be due to local terrain undulations or jamming during track transmission. Fig. 15(c)(ii) shows the variation of the comprehensive energy-saving rate. $\eta_{\text{com}-\text{RT}}$ has been in a nonenergy-saving state during the first part of experiment. This was due to the assistance force of the sail on USTM, which caused the center of gravity to shift to the right, resulting in an increase in the required driving force for the right track. The comprehensive energy-saving rate of the entire climbing process was 12%.

3) *Downhill Terrain Experiment:* We controlled the robots to go downhill in FSTM, USTM, FSSM, and USSM, as shown in Fig. 16(a)–(d). The slope was 10°. The robot's speed was about 1.2 m/s. The wind direction and speed information under USTM were collected, as shown in Fig. 17(a). During the downhill process, the wind direction angle did not change significantly, ranging from 40°–80°, and the average wind speed was about 2.5 m/s. The corresponding sail position angle varies between 50° and 100°, and the trend was consistent with the wind direction angle. The assistance force varies between 5 and 25 N.

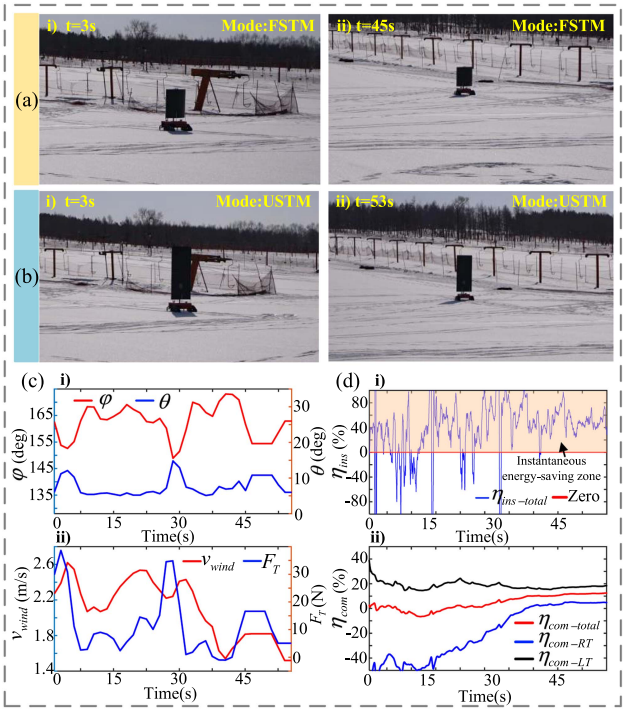

Fig. 15. Climbing terrain experiment results. (a) Process of climbing terrain motion under FSTM. (b) Process of Climbing terrain motion under USTM. (c)(i) Wind direction and corresponding sail position angles under USTM. (c)(ii) Wind speed and corresponding sail assistance force under USTM. (d)(i) Variation of instantaneous energy-saving rate η_{ins}. (d)(ii) Variation of the comprehensive energy-saving rate $\eta_{\text{com-total}}$, $\eta_{\text{com-RT}}$, $\eta_{\text{com-LT}}$.

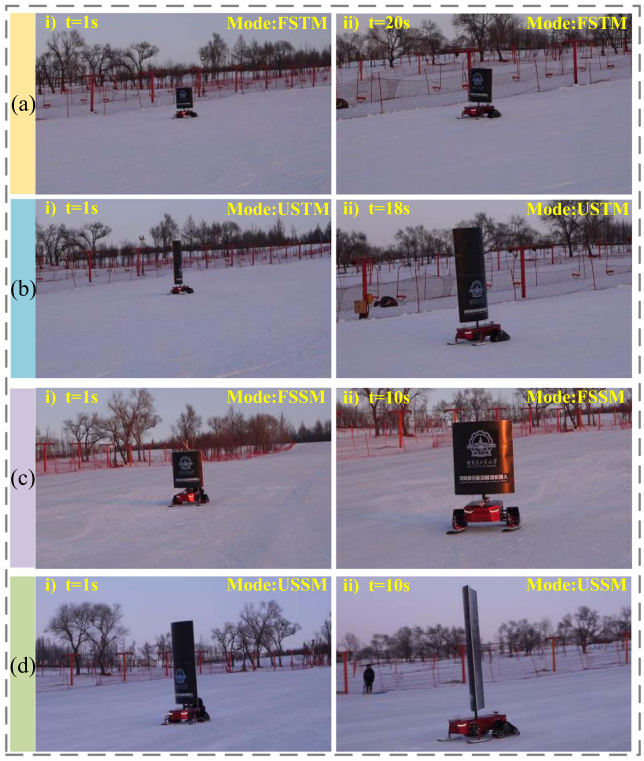

Fig. 16. Downhill terrain experiment. (a) Process of downhill terrain motion under FSTM. (b) Process of downhill terrain motion under USTM. (c) Process of downhill terrain motion under FSSM. (d) Process of downhill terrain motion under USSM.

Fig. 17(b)(i) represents the instantaneous energy-saving rates $\eta_{\text{ins}}^{\text{USTM}}$, $\eta_{\text{ins}}^{\text{USSM}}$, and $\eta_{\text{ins}}^{\text{FSSM}}$ under USTM, FSSM, and USSM, respectively. It can be clearly seen that the instantaneous energy-saving rate of FSSM and USSM sliding modes is over 90% throughout the entire process. This is due to the fact that the sliding process did not require the involvement of tracks at all. The instantaneous energy saving rate of USTM is below 20%.

Fig. 17(b)(ii) represents the variation of the comprehensive energy-saving rate. The comprehensive energy-saving rates of FSSM and USSM were 95% and 97%, respectively, while comprehensive energy-saving rate of USTM is only 20%. This further confirms that the energy-saving effect brought by the sliding mode is more significant.

C. Multimode Motion Comprehensive Energy-Saving Experiment

To verify the energy-saving effect under multiple motion modes, we controlled the robot's motion on a rectangular slope similar to that in the simulation. One of the tests used FSTM mode, as shown in Fig. 18(a). In another test, the robot achieved motion mode selection through energy-saving control, as shown in Fig. 18(b). In multimode motion, the robot was USTM in Path 1, Path 2, Path 3 and USSM in Path 4. The robot maintained a constant speed of 1 m/s.

We recorded the trajectory and yaw angle information in two modes, as shown in Fig. 18(c). The exercise information of

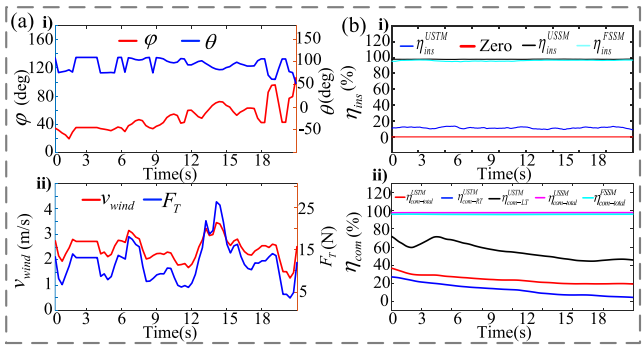

Fig. 17. Downhill terrain experiment results. (a)(i) Wind direction and corresponding sail position angles under USTM. (a)(ii) Wind speed and corresponding sail assistance force under USTM. (b)(i) Variation of instantaneous energy-saving rate $\eta_{\text{ins}}^{\text{USTM}}$, $\eta_{\text{ins}}^{\text{USSM}}$, $\eta_{\text{ins}}^{\text{FSSM}}$. (b)(ii) Variation of the comprehensive energy-saving rate $\eta_{\text{com-total}}^{\text{USTM}}$, $\eta_{\text{com-total}}^{\text{USSM}}$, $\eta_{\text{com-total}}^{\text{FSSM}}$.

the two tests remained basically consistent. In the multimode motion, the range of wind direction angle variation was relatively large, ranging from 10°–140°, with an average wind speed of about 3 m/s. According to the energy-saving control method, the sail position angle varied between 40° and 100°, and the trend was consistent with the wind direction angle. The assistance force varied between 5 and 30 N and followed the trend of wind speed.

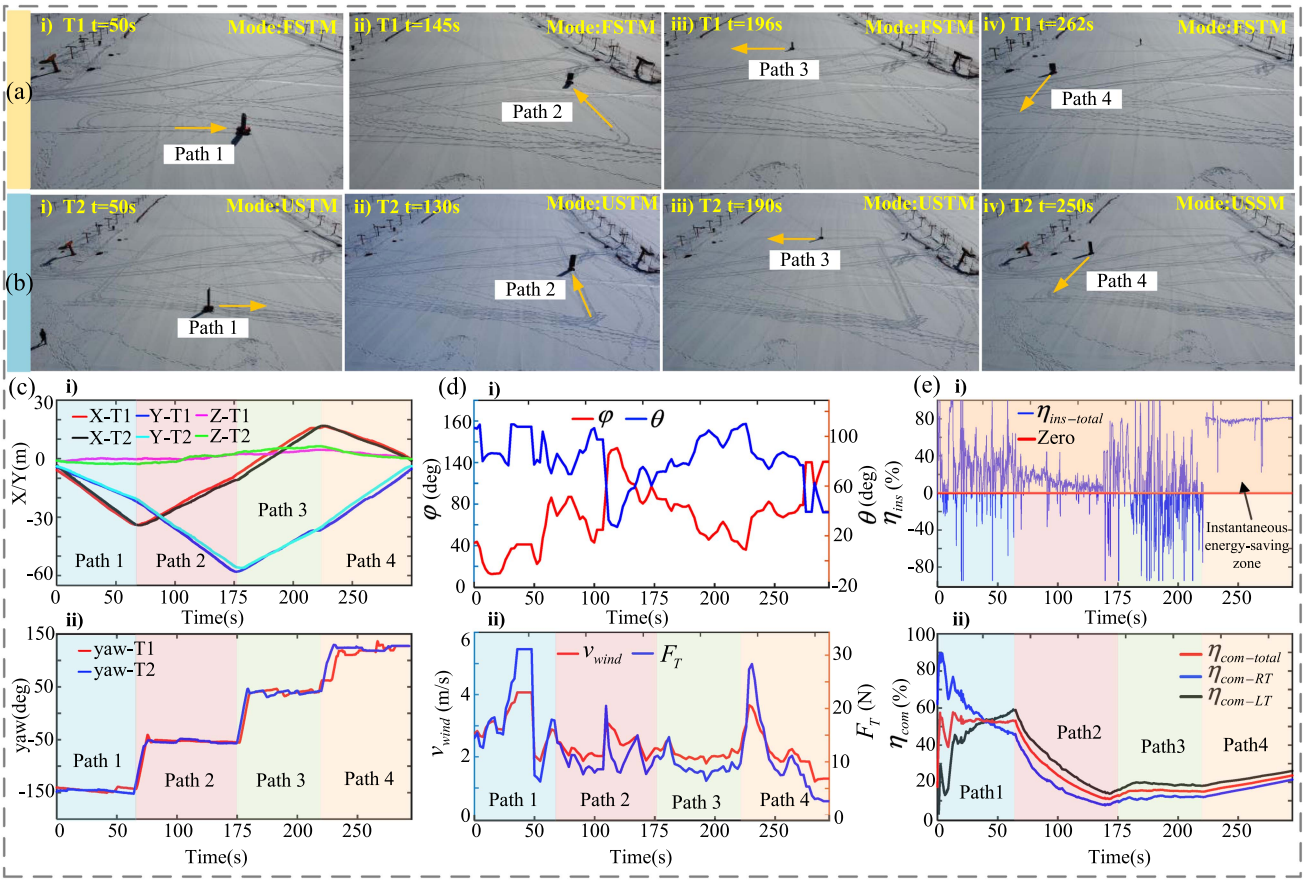

Fig. 18. Multimode motion comprehensive energy-saving experiment results. (a) Process under FSTM. (b) Process under Multimode motion. (c) Trajectory and yaw angle information in FSTM and multimode motion. (d)(i) Wind direction and corresponding sail position angles under multimode motion. (d)(ii) Wind speed and corresponding sail assistance force under multimode motion. (e)(i) Variation of instantaneous energy-saving rate η_{ins}. (e)(ii) Variation of the comprehensive energy-saving rate $\eta_{\text{com}-totol}, \eta_{\text{com}-\text{RT}}, \eta_{\text{com}-\text{LT}}$.

The fluctuations of η_{ins} in path 1 and path 3 were relatively large, which may be caused by local terrain undulations and jamming, but most of the time η_{ins} was in the instantaneous energy-saving zone. η_{ins} was significantly lower in the process of path 2 compared to other paths. This was because path 2 was in the climbing process and requires greater driving force from the tracks. In the process of path 4, η_{ins} basically reaches 80%. This was because Path 4 has switched to USSM and no longer required tracks to provide power.

Fig. 18(c)(ii) shows the variation of the comprehensive energy-saving rate. $\eta_{\text{com}-\text{total}}$ significantly decreased in Path 2, remained stable in Path 3, and continued to climb in Path 4. The $\eta_{\text{com}-\text{total}}$ in multimode motion is about 24%.

D. Discussion on Experimental Results

The energy-saving experimental results of independent modes under different terrains and modes have been summarized, as shown in Table III.

FSTM is the most conventional exercise mode with the highest energy consumption, but it can adapt to any environment. The energy-saving rate of FSTM is set 0 for comparison with other modes.

TABLE III
ENERGY SAVING RATES OF MULTIMODES IN DIFFERENT TERRAINS

Terrain	FSTM	USTM	FSSM	USSM
Flat terrain	0	17.1%	-	-
Climbing terrain		12%	-	-
Downhill terrain		20%	95%	97%

USTM can also adapt to most terrains, with an efficiency of around 20% for its sail assistance. The smallest on climbing terrain and the largest on downhill terrain.

Both FSSM and USSM have energy-saving rates of over 95%, with USSM being even higher. This is because the sliding mode does not require tracks to provide power. Although the sliding mode is very energy efficient, it is not suitable for all environments. When the sail assistance force does not reach to drive robot, it is difficult to select on flat terrain, climbing terrain, etc.

The comprehensive energy-saving experiment of multimodes motion shows that in downhill environments, due to the force of gravity, it is easy to switch to sliding mode to improve energy

efficiency. The comprehensive energy-saving rate of the entire process is about 24%, which is close to the energy-saving rate of 21% obtained from our simulation under a wind speed of 3 m/s and a slope of 10°. The differences may come from unstable wind speeds, locally undulating terrain, and so on. But this does not affect our verification of the effectiveness of energy-saving motion control framework.

VI. Conclusion

This article proposed a multimodes motion polar robot, which achieves energy saving by switching modes through foldable sails and transformable tracks. The unfolded sail generates assistance and folded sail ensures stability without assistance. The sail shape is designed by symmetrizing the NACA0018 sail. The influence of variations in sail parameters on the aerodynamics performance is compared and discussed. By modeling the foldable sail, the relationship between assist performance and wind direction angle and attack angle is obtained. Fluid-structure coupling analysis under extreme climate conditions confirms the robustness of the design. The transformation of the track realizes the switching between traction and sliding modes. By separating the teeth chain from the track chain, the teeth chain extends in traction mode and retracts in sliding mode. The track traction comprehensive performance based on teeth effect is modeled. Increasing the height and width of track teeth improves traction performance. The kinematics of steering and braking process and system dynamics are modeled. The stability constraints under different terrain conditions are provided. A energy-saving control framework under multimodes motion is proposed, and the energy-saving effect has been verified through simulation.

The robot maneuverability was validated through terrain adaptability tests conducted on compacted snow, soft snow, and mixed snow-ice surfaces. It successfully traversed ice cracks up to 30-cm high. The energy-saving benefits of sail assistance and traction-sliding switching were evaluated in independent mode experiments on flat, uphill, and downhill terrains. USTM can adapt to the most terrain and has the highest energy saving rate of 20% when downhill. The energy-saving rate of FSSM and USSM are 95% and 97%, respectively, which are not suitable for all environments. In multimode motion comprehensive energy-saving experiment, the comprehensive energy-saving rate of the entire process is about 24%, which is close to the energy-saving rate of 21% obtained in simulation, verifying the effectiveness of the energy-saving motion control method.

In summary, the polar robot achieves energy efficiency through multimode motion switching. Under the constraints of limited energy supply in future Antarctic missions, the energy-saving capability of the polar robot will enable longer-duration and larger-scale scientific exploration.

References

[1] E. Hanna, "The role of Antarctic sea ice in global climate change," *Prog. Phys. Geography*, vol. 20, no. 4, pp. 371–401, 1996.

[2] L. Skinner, L. Menviel, L. Broadfield, J. Gottschalk, and M. Greaves, "Southern ocean convection amplified past Antarctic warming and atmospheric CO_2 rise during Heinrich stadial 4," *Commun. Earth Environ.*, vol. 1, no. 1, 2020, Art. no. 23.

[3] D. Raynaud and J. M. Barnola, "An Antarctic ice core reveals atmospheric Co2 variations over the past few centuries," *Nature*, vol. 315, no. 6017, pp. 309–311, May 1985.

[4] K. R. Clem et al., "Record warming at the south pole during the past three decades," *Nature Climate Change*, vol. 10, no. 8, pp. 762–770, Aug. 2020.

[5] P. Xiaoping, L. Haiyan, and Z. Xi, "Selecting suitable sites for an Antarctic research station: A case for a new Chinese research station," *Antarctic Sci.*, vol. 26, no. 5, pp. 91–99, 2014.

[6] L. Bingrui, Q. Weijia, G. Jingxue, Z. Yiwen, and L. Jianhong, "Experimental application of intelligent robot technology in Antarctic scientific expedition," *Chin. J. Polar Res.*, vol. 21, no. 1, pp. 91–99, 2010.

[7] D. S. Apostolopoulos, M. D. Wagner, B. N. Shamah, L. Pedersen, K. Shillcutt, and W. L. Whittaker, "Technology and field demonstration of robotic search for Antarctic meteorites," *Int. J. Robot. Res.*, vol. 19, no. 11, pp. 1015–1032, 2000.

[8] M. Wagner, D. Apostolopoulos, K. Shillcutt, B. Shamah, R. Simmons, and W. Whittaker, "The science autonomy system of the nomad robot," in *Proc. IEEE Int. Conf. Robot. Automat.*, vol. 2, 2001, pp. 1742–1749.

[9] E. L. Akers, H. P. Harmon, R. S. Stansbury, and A. Agah, "Design, fabrication, and evaluation of a mobile robot for polar environments," in *Proc. IEEE Int. Geosci. Remote Sens. Symp.*, vol. 1, 2004, p. 112, doi: 10.1109/IGARSS.2004.1368957.

[10] R. S. Stansbury, E. L. Akers, H. P. Harmon, and A. Agah, "Survivability, mobility, and functionality of a rover for radars in polar regions," *Int. J. Control Automat. Syst.*, vol. 2, pp. 343–353, 2004.

[11] C. Chen, C. Bu, Y. He, and J. Han, "Design, implementation and experimental tests of a new generation of Antarctic rover," in *Proc. IEEE Int. Conf. Robot. Biomimetics*, 2012, pp. 2144–2149.

[12] C. Cheng, B. Chunguang, H. Yuqing, and H. Jian-da, "Environment modeling for long-range polar rover robots," *Chin. Sci. Bull.*, vol. 58, pp. 75–82, 2013.

[13] E. W. Wolff and D. A. Peel, "Night-time measurements of astronomical seeing at Dome A in Antarctica," *Nature*, vol. 313, pp. 535–540, Feb. 1985.

[14] A. V. Vesman, A. A. Ershova, E. N. Litina, and P. V. Chukmasov, "Assessment of marine litter on the fields peninsula, King George island, Antarctica," *Mar. Pollut. Bull.*, vol. 200, 2024, Art. no. 116164.

[15] J. Lever, A. Streeter, and L. Ray, "Performance of a solar-powered robot for polar instrument networks," in *Proc. IEEE Int. Conf. Robot. Automat.*, 2006, pp. 4252–4257.

[16] L. E. Ray, J. H. Lever, A. D. Streeter, and A. D. Price, "Design and power management of a solar-powered cool robot for polar instrument networks: Research articles," *J. Field Robot.*, vol. 24, no. 7, pp. 581–599, 2007.

[17] D. Wettergreen et al., "First experiment in sun-synchronous exploration," in *Proc. IEEE Int. Conf. Robot. Automat.*, vol. 4, 2002, pp. 3501–3507.

[18] G. Hajos, J. Jones, A. Behar, and M. Dodd, "An overview of wind-driven rovers for planetary exploration," in *Proc. 43rd AIAA Aerosp. Sci. Meeting Exhibit*, 2005, AIAA-2005 244. [Online]. Available: https://arc.aiaa.org/doi/abs/10.2514/6.2005-244

[19] T. Wang, "Design and field test of a rover robot for Antarctic based on renewable energy," *J. Mech. Eng.*, vol. 49, pp. 21–30, 2013.

[20] H. Yihuai, *Sail-Assisting Technology for Modern Ships*. Shanghai, China: Shanghai Jiao Tong Univ. Press, 2018.

[21] M. Biancolini, I. Viola, and M. Riotte, "Sails trim optimisation using CFD and RBF mesh morphing," *Comput. Fluids*, vol. 93, pp. 46–60, 2014. [Online]. Available: https://www.sciencedirect.com/science/article/pii/S0045793014000140

[22] L. Guo, G. Liu, Y. Luo, P. Jiang, and J. Zhao, "A wind-electric hybrid polar roaming robot: Design, modeling, and experiments," *J. Field Robot.*, vol. 41, no. 1, pp. 131–143, 2024.

[23] B. M. G., *Introduction to Terrain-Vehicle System*. Ningbo, China: China Mach. Press, 1969.

[24] S. Shoop, P. Richmond, and J. Lacombe, "Overview of cold regions mobility modeling at CRREL," *J. Terramechanics*, vol. 43, no. 1, pp. 1–26, 2006.

[25] Y. Luo, G. Liu, L. Guo, Y. Zhu, and J. Zhao, "Scalable wing sailing and snowboarding enhance efficient and energy-saving mobility of polar robot," *IEEE/ASME Trans. Mechatron.*, vol. 29, no. 5, pp. 3833–3844, Oct. 2024.

[26] H. Zhen, Z. Yongsheng, and Z. Tieshi, *Advanced Spatical Mechanism*. Beijing, China: Higher Educ. Press, 2014.

[27] J. H. Lever, D. Denton, G. E. Phetteplace, S. D. Wood, and S. A. Shoop, "Mobility of a lightweight tracked robot over deep snow," *J. Terramechanics*, vol. 43, no. 4, pp. 527–551, 2006.

[28] F. Yijie, O. Yi, and H. Jun, "Analysis of steering dynamics model of special robot on mechamical Antarctic soft ground," *J. Nanjing Univ. Sci. Technol.*, vol. 47, no. 5, pp. 611–618, 2023.

Yongsheng Luo received the B.E. and M.E. degrees in mechanical engineering from the Harbin Institute of Technology, Harbin, China, in 2021 and 2023, respectively, where he is currently working toward the Ph.D. degree in mechanical engineering with the State Key Laboratory of Robotics Technology and System.

His research interests include configuration design and motion control of special environment robots.

Zhaokun Guo received the B.E. degree in agricultural mechanization and automation from the Northeast Agricultural University, Harbin, China, in 2022. He is currently working toward the M.E. degree in robotics engineering with the Harbin Institute of Technology.

His research interests include robot configuration design and process equipment design

Tao Liu received the B.E. and M.E. degrees in mechanical engineering, in 2020 and 2022, respectively, from the Harbin Institute of Technology, Harbin, China, where he is currently working toward the Ph.D. degree in mechanical engineering with the State Key Laboratory of Robotics Technology and System.

His research interests include configuration design and motion control of special environment robots.

Kaixuan Li received the B.E. and M.E. degrees in mechanical engineering, in 2021 and 2023, respectively, from the Harbin Institute of Technology, Harbin, China, where he is currently working toward the Ph.D. degree in mechanical engineering with the State Key Laboratory of Robotics Technology and System.

His research interests include configuration design and motion control of special environment robots.

Jinnong Liao received the B.E. degree in mechanical engineering from the Faculty of Materials and Manufacturing, Beijing University of Technology, Beijing, China, in 2021. He is currently working toward the Ph.D. degree in mechanical engineering with the School of Mechatronics Engineering, Harbin Institute of Technology, Harbin, China.

His research interests include robotics, complex mechanism design methods, and system integration.

Lefan Guo received the B.E. degree in mechanical engineering, in 2021, from the Harbin Institute of Technology, Harbin, China, where he is currently working toward the M.E. degree with the State Key Laboratory of Robotics Technology and System.

His research interests include configuration design and motion control of special environment robots.

Yanhe Zhu (Senior Member, IEEE) received the B.E. and Ph.D. degrees in mechatronics engineering from the Harbin Institute of Technology (HIT), Harbin, China, in 1998 and 2004, respectively.

He is currently a Professor and a Ph.D. Supervisor with the School of Mechatronics Engineering, HIT, where he is also the Deputy Director of the State Key Laboratory of Robotics and System. His research interests include reconfigurable modular robots and robotic exoskeletons.

Gangfeng Liu (Senior Member, IEEE) received the B.E., M.E, and Ph.D. degrees in mechatronics engineering from the Harbin Institute of Technology (HIT), Harbin, China, in 2003, 2005 and 2010, respectively.

He is currently a Professor and a Ph.D. Supervisor with the School of Mechatronics Engineering, HIT, where he is currently the member of the State Key Laboratory of Robotics and System. His research interests include motion control of special environment robots.

Jie Zhao (Senior Member, IEEE) was born was born in Jilin, China, in 1968. He received the B.E., M.E., and Ph.D. degrees in mechatronics engineering from the Harbin Institute of Technology, Harbin, China, in 1990, 1993, and 1996, respectively.

He has been a Professor with the State Key Laboratory of Robotics and System, Harbin Institute of Technology, since 2001. He is the Leader of the Subject Matter Expert Group of Intelligent Robot in National 863 Program supervised by the Ministry of Science and Technology of China. His research interest includes design, modeling and control of industrial robots and bionic robots.